applied sciences

MDPI

Article

Consequences of Deep Rolling at Elevated Temperature on Near-Surface and Fatigue Properties of High-Manganese TWIP Steel X40MnCrAl19-2

Thomas Wegener *, Marcel Krochmal, Torben Oevermann and Thomas Niendorf

Institute of Materials Engineering—Metallic Materials, University of Kassel, Mönchebergstraße 3, 34125 Kassel, Germany; krochmal@uni-kassel.de (M.K.); torben.oevermann@gmx.de (T.O.); niendorf@uni-kassel.de (T.N.)
* Correspondence: t.wegener@uni-kassel.de

Abstract: Due to pronounced work-hardening induced by the complex interplay of deformation mechanisms such as dislocation slip, twinning and/or martensitic phase transformation, high-manganese steels represent a class of materials well-suited for mechanical surface treatment. In the present study, the fatigue behavior of a high-mangsanese steel showing twinning-induced plasticity (TWIP) effect at room temperature (RT) was investigated after deep rolling at 550 °C. Results are compared to a former study discussing the behavior after RT deep rolling. Evolution of the near-surface microstructure was analyzed by scanning electron microscopy (SEM), microhardness measurements and residual stress depth profiles obtained by X-ray diffraction (XRD). Both uniaxial tensile tests and uniaxial tension-compression fatigue tests have been conducted in order to rationalize the macroscopic material behavior. Following deep rolling at 550 °C, SEM measurements employing electron backscatter diffraction (EBSD) revealed a heavily deformed surface layer as well as localized deformation twinning. Specimens showed inferior hardness and residual stress depth profiles when compared to RT deep rolled counterparts. Tensile tests indicated no difference between the conditions considered. Fatigue properties however were improved. Such behavior is rationalized by a more stable residual stress state induced by dynamic strain aging.

Keywords: high-manganese steel; deep rolling; TWIP; near-surface properties; residual stresses; residual stress stability; fatigue behavior

Citation: Wegener, T.; Krochmal, M.; Oevermann, T.; Niendorf, T. Consequences of Deep Rolling at Elevated Temperature on Near-Surface and Fatigue Properties of High-Manganese TWIP Steel X40MnCrAl19-2. *Appl. Sci.* **2021**, *11*, 10406. https://doi.org/10.3390/app112110406

Academic Editors: Luís Coelho and Joao Nobre

Received: 13 October 2021
Accepted: 2 November 2021
Published: 5 November 2021

1. Introduction

Due to their improved formability and crash performance, advanced high-strength steels (AHSS) have been in the focus of the mobility sector for more than two decades. The group of AHSS generally includes steels with yield strengths (YS) and ultimate tensile strengths (UTS) exceeding 300 and 600 MPa, respectively [1,2]. AHSS can be classified into several different generations. The first generation of AHSS, mainly steels with a ferritic structure, include dual-phase (DP) steels and transformation-induced plasticity (TRIP) steels with retained austenite, as well as complex phase (CP) and martensitic steels [3]. However, steels of the first AHSS generation are characterized by a high strength–high ductility discrepancy, i.e., a decreasing formability with an increase in strength. With the ongoing advance of globalization, a steady increase in the requirements being considered for new materials, material combinations and manufacturing processes can be recognized. Besides the constantly developing automation technology, light-weight design is often referred to as the innovation driver of the industry [4]. Current development is therefore focusing in particular on increasing resource efficiency, thus contributing to sustainability of products and processes. As a result, the simultaneous demand for materials with high strength and sufficiently good formability led to the development of the second AHSS generation, i.e., austenitic steels with high manganese contents [3]. In addition to nanoparticle-hardened, martensitic TRIP and twinning-induced plasticity (TWIP) steels,

as well as the subgroup of density-reduced light-weight steels realized by adding high aluminum contents, TWIP and TRIP steels in particular have been in focus of scientific and commercial interest in the group of high-manganese steels (HMnS) due to their outstanding mechanical properties under monotonic loading [3,5]. TWIP and TRIP HMnS are characterized by high strengths ranging from 500 to 1200 MPa and a concomitantly excellent formability of 40–70%, resulting in strength–ductility products between 40,000–50,000 MPa-% [6,7]. As this value is limited to about 20,000 MPa-% for conventional steels, it is often used to express the high work-hardening potential of TWIP/TRIP steels as well as their excellent energy absorption capability [8]. In addition, HMnS TWIP and TRIP steels are characterized by a lower density of about 6.8–7.3 g/cm^3 compared to conventional steel counterparts [9,10], eventually allowing for the development of weight-reduced crash-relevant body structures leading to a reduction in fuel consumption and CO_2 emissions. The group of austenitic HMnS, being firstly discovered by the work of Sir Robert Hadfield in 1888 [11], includes alloys with a manganese content between 10 and 35 wt.% [6,7,12]. The exceptional mechanical properties of these alloys can be attributed to the activation of multiple deformation mechanisms. Besides planar dislocation slip, deformation-induced twinning (TWIP-effect) as well as a mechanically driven solid–solid phase transformation from γ-austenite to either α'-martensite or ε-martensite (TRIP-effect) can prevail [13,14]. The martensitic transformation is strongly affected by the thermodynamic stability of the phases being present and can therefore take place directly ($\gamma \rightarrow \varepsilon$, $\gamma \rightarrow \alpha'$) or in multiple transformation steps ($\gamma \rightarrow \varepsilon \rightarrow \alpha'$). The contribution of the partially competing deformation mechanisms thereby depends on the level of the stacking fault energy (SFE) [13]. Due to the widely scattered literature data (cf. [14–21]), a clear delimitation of the deformation mechanisms as a function of the SFE turns out to be difficult. Limits for the activation of the individual mechanisms can rather be regarded as threshold values of transition regions, in which several deformation mechanisms can also be activated in parallel [19,22]. Despite significantly differing information, a range of mean SFEs between 20 and 50 mJ/m^2 can be deduced from the literature, in which the TWIP effect is the preferred deformation mechanism [1,23,24]. While deformation-induced twinning is replaced by the TRIP effect in the range of low SFEs below 20 mJ/m^2, dislocation slip represents the dominant deformation mechanism in the range of high SFEs > 50 mJ/m^2 [25]. In this area of high SFEs, another subgroup of HMnS, the aforementioned density-reduced light-weight steels, have gained significant attention in recent investigations [26]. Following the TWIP and TRIP effect, new deformation mechanisms, namely the shear-band-induced plasticity (SIP) [27], the microband-induced plasticity (MBIP) [28], the slip-band refinement-induced plasticity (SRIP) [29] or the dynamic slip band refinement (DSBR) [30], have been reported. A detailed summary of these deformation mechanisms is presented in [31]. In HMnS, the SFE itself is strongly influenced by the alloying concept as well as the deformation temperature, highlighting the influence of these two parameters on the active deformation mechanisms [5,13,14,18,32]. According to the literature, the alloying elements can primarily be divided into elements increasing the SFE (C, Al, Ni and Cu) and elements that cause a decrease in the SFE (Cr and Si). The main alloying element Mn has a parabolic influence on the SFE in binary Fe-Mn alloys as well as in the Fe-Mn-C alloy system, i.e., the SFE decreases with increasing Mn content up to about 13 wt.% and then increases again with further addition of Mn [32–35]. In addition, the influence of Ni on the SFE shows different tendencies depending on the chemical composition of the base material as well as the range of the Ni concentration [32]. Furthermore, the deformation temperature also has a significant effect on the resulting SFE as it increases with higher temperatures [5]. Using the thermodynamic approach of Olsen and Cohen [36], Grässel et al. [37] for example were able to determine the Gibbs free energy and, hence, the SFE as a function of temperature for an Fe-Mn-Si-Al alloy, demonstrating a proportional increase in the SFE with increasing temperature. The influence of temperature on the SFE was additionally discussed by Rüsing et al. [38] for the austenitic X40MnCrAl19-2 TWIP steel, the alloy being in focus of the present study. Investigating the effect of pre-deformation temperature on the fatigue

behavior, the authors showed that pre-deformation at room temperature (RT) resulted in deformation-induced twinning, whereas for a pre-deformation temperature of −196 °C, the TWIP-effect was accompanied by the formation of ε- as well as α′-martensite. An elevated pre-straining temperature of 400 °C led to the suppression of both effects.

Due to their outstanding mechanical properties as well as the possibility to overcome the strength–ductility trade-off, HMnS exhibit a great potential for the development of components for the mobility sector, e.g., crash-relevant body structures. As many of the intended applications of these steels will be subjected to cyclic loadings during their service life, the fatigue behavior is of utmost importance. As a result, the crack growth behavior as well as the fatigue properties in different regimes, including low-cycle and high-cycle fatigue (LCF/HCF) regimes, have been investigated in several studies focusing on the influences of twinning and martensitic phase transformation, i.e., TWIP- and TRIP-effect, as well as the influence of grain size, strain rate, deformation temperature and pre-deformation on the fatigue behavior. A detailed literature survey on these studies is presented in [39].

Generally, the surface condition of a component has a significant influence on the fatigue behavior as the surface represents the area being subjected to the highest stresses during cyclic loading. In addition to the load distribution, geometrically necessary notches as well as corrosion or wear often lead to crack initiation directly at the surface or within the near-surface area [40,41]. Thus, the condition of the near-surface layer determines the properties, i.e., the surface integrity (SI), of a component under cyclic loading or tribological and corrosive stresses, amongst others. Mechanical surface treatment processes are well-known for establishing near-surface layers of a component that are characterized by high compressive residual stresses, increased hardness due to strain hardening and a smooth surface appearance, depending on the respective treatment process used [40,42–44]. Furthermore, deformation-induced twinning or phase transformation, exemplarily shown in [39,45–47], can be obtained as a result of high plastic deformation. In particular, residual stresses are of paramount importance for the service life of structural components. While compressive residual stresses increase the service life, tensile residual stresses, which are a direct result of many technological processes such as welding, have a detrimental effect as they promote crack initiation and accelerate crack growth [48–52]. Therefore, evaluation of residual stresses by experimental or theoretical analysis is mandatory for the assessment of components realized by different machining and manufacturing processes [53,54]. Deep rolling and shot peening represent the most common mechanical surface treatment processes, however, a large variety of other techniques such as hammering, grinding, brushing, needle or water peening have been established [42]. Furthermore, several of these treatments can be conducted at differing temperatures, eventually promoting additional modifications of the near-surface layer. As a result of the pronounced work-hardening ability detailed above, HMnS are suitable candidate materials for mechanical surface treatment processes. However, only a few studies investigating the effect of mechanical surface treatments and, thus, the effect of residual stresses, hardness and roughness on the SI of HMnS TWIP and TRIP steels, can be found in the literature [47,55–57]. In a previous study, the evolution of residual stresses, microstructure and cyclic performance of the X40MnCrAl19-2 TWIP steel after deep rolling at RT, −196 and 200 °C, was investigated by the authors' group [39]. Following deep rolling at RT and 200 °C, twinning in the near-surface area was detected to a similar extent, indicating that the increase in temperature and, thus, in the SFE was not high enough to suppress the TWIP-effect. In contrast, cryogenic deep rolling at −196 °C led to a solid–solid phase transformation, promoting the formation of ε-martensite in the near-surface layer. The highest residual stresses with a maximum of −800 MPa accompanied by high hardness values up to 475 HV0.1 were reported for the condition being deep rolled at 200 °C. Compared to the initial state, fatigue properties in the HCF regime were improved irrespective of the deep rolling temperature. However, the martensitic phase transformation induced by cryogenic deep rolling was shown to have a negative impact on the fatigue performance, at least at relatively high loading amplitudes.

This was rationalized by an increased plastic deformation as well as microstructural notch effects in the two-phase region established in the near-surface area. In line with the similar microstructures, fatigue properties of the conditions deep rolled at RT and 200 °C revealed only minor differences. Still, data indicated a slightly improved performance at high stress amplitudes after deep rolling at elevated temperature.

In order to further analyze the consequences of deep rolling at elevated temperature on near-surface and fatigue properties of the TWIP steel X40MnCrAl19-2, the present work, a follow-up study to the work of Oevermann et al. [39], was conducted. To tackle prevailing research gaps, deep rolling was carried out at an elevated temperature of 550 °C. In addition to the analysis of the near-surface microstructure and the residual stress state by means of electron backscatter diffraction (EBSD) and X-ray diffraction (XRD) respectively, results of microhardness measurements and uniaxial tensile tests are assessed. The fatigue performance in the HCF regime was investigated by fully reversed tension-compression tests. The results are critically discussed based on microstructural evolution as well as fracture surface analysis. Finally, the residual stress stability at half-life for conditions deep rolled at room and elevated temperature was studied.

2. Material and Methods

The material in focus is the high-Mn austenitic TWIP steel X40MnCrAl19-2 (precidur® H-Mn LY) provided by thyssenkrupp Hohenlimburg GmbH (Hagen, Germany). As reported in [39], the initial state is characterized by an average hardness of 250 HV as well as a homogenous microstructure with an average grain size of about 20 µm and a high fraction of recrystallization twins. Furthermore, tensile tests disclosed a YS and UTS of about 400 and 880 MPa respectively, demonstrating the high work-hardening potential of the material, as well as an elongation at fracture of approximately 52%.

The present work reports a follow-up study. For detailed information on the experimental setup, i.e., specimen preparation, machines and parameters used, the reader is referred to [39] for the sake of brevity. In addition to RT deep rolling, deep rolling at an elevated temperature of 550 °C was performed for the first time in the present study. According to the previous results, a deep rolling force of 855 N was chosen. Conditions deep rolled at RT and 550 °C are referred to as dr_855_RT and dr_855_550 °C in the remainder of the manuscript. In order to expand the fatigue database shown for RT deep rolling in [39] and in order to conduct a minimum of at least four tests for all stress amplitudes considered, several additional fatigue tests were also performed for the dr_855_RT condition.

The residual stress stability at half-life was investigated for 5 different stress amplitudes, i.e., 425, 460, 480, 500 and 540 MPa. Based on data obtained, the arithmetic mean of the number of cycles to failure was calculated from all tests being conducted on a stress level considered. Prior to the fatigue test, residual stress values were determined at the direct surface in the center of the gauge length of the specimen. The spot of the measurement was marked by a color marker. Subsequently, the specimens were fatigued to the averaged half-life before surface residual stresses were measured again at the marked spot. Additionally, post-fatigue residual stress depth profiles were determined for the lowest and highest stress amplitudes of 425 and 540 MPa, respectively. All tests that have either been conducted within the present work or recompiled from [39] are summarized in Table 1.

Table 1. Summary of the conducted and recompiled tests for the different conditions considered.

	EBSD	Hardness	Residual Stress Profiles	Tensile Tests	Fatigue Tests	Residual Stress Stability	Fracture Surface Analysis
dr_855_RT	-	Recompiled from [39]	Recompiled from [39]	Recompiled from [39]	Partly recompiled from [39]	X	-
dr_855_550 °C	X	X	X	X	X	X	X

3. Results and Discussion

3.1. Near-Surface Properties

Microstructural analysis of the near-surface layer after deep rolling at an elevated temperature of 550 °C was carried out by EBSD. Figure 1 shows a representative EBSD inverse pole figure (IPF) map with superimposed image quality (IQ). Similar to the initial state and the dr_855_RT condition shown in [39], the overall microstructure shows no preferred orientation. Furthermore, grains are pervaded with sub-grain structures. In line with the conditions detailed above, grain refinement, being numerously reported for mechanical surface treatments such as deep rolling [42], becomes obvious in the near-surface layer. Despite the increased deep rolling temperature of 550 °C and a corresponding increase in the SFE, mechanical twins can be still seen in some grains of the dr_855_550 °C condition, i.e., in an area of about 50 µm below the surface. Although these twins are present to a lesser extent compared to the dr_855_RT condition, it can be deduced that an increase of the deep rolling temperature to 550 °C is still not sufficient to fully suppress the TWIP effect here. In contrast to the results of Rüsing et al. [38], revealing no deformation twinning after uniaxial tensile testing at a deformation temperature of 400 °C, this observation clearly demonstrates that the multiaxial stress state induced by deep rolling is still able to activate the TWIP effect despite the even higher process temperature of 550 °C. Nevertheless, besides the low extent of deformation-induced twinning, the austenite grains seem to be mainly deformed by dislocation slip. This can be deduced from the high amount of EBSD zero solutions displayed in black in the direct vicinity of the surface, clearly indicating high dislocation densities in a region about 15–20 µm below the surface.

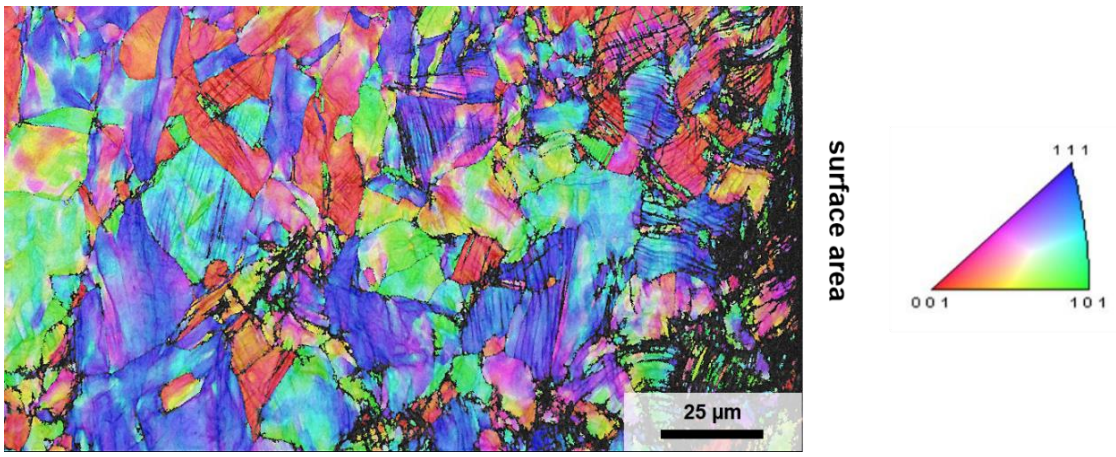

Figure 1. IPF map with superimposed IQ depicting the near-surface microstructure following deep rolling at 550 °C using a deep rolling force of 855 N. Color coding with respect to loading direction is in accordance with the standard triangle shown on the right.

In line with the literature detailed before, deep rolling at 550 °C leads to increased surface layer hardness when compared to the initial state (recompiled from [39]). This is demonstrated by the hardness distribution in the near-surface area, as shown in Figure 2. A peak hardness value of approximately 425 HV0.2 has been measured at a distance of 0.08 mm to the surface for the dr_855_550 °C condition, which is lower than the corresponding peak hardness of the dr_855_RT specimen examined in the prior work by Oevermann et al. [39]. This trend continues until both graphs intersect at a depth of 0.45 mm. Afterwards, dr_855N_550 °C shows higher values in all cases. The different work-hardening effects after deep rolling at RT and 550 °C are further illustrated by the integral width distributions depicted in Figure 3c,d, where the dr_855N_550 °C condition is generally characterized by lower values than dr_855N_RT in both longitudinal and circumferential directions. These observations can be attributed to stress relaxation induced by recovery effects at the given temperature. Such effects are able to soften the material, as numerously

shown in the literature [58–62]. Here, recovery effects mainly set in in the severely deformed near-surface area of the specimen, leading to a reduction in the hardness values. At larger distances from the surface, the positive effects of the warm deep rolling, i.e., a more pronounced work-hardening accompanied by an increase in hardness, appear to overcome the effects related to the recovery processes, eventually explaining the intersection point of the dr_855_550 °C and dr_855_RT conditions displayed in Figure 2. As Oevermann et al. [39] pointed out, the increased depth effect can be attributed to the generally decreased resistance of the material against plastic deformation [63].

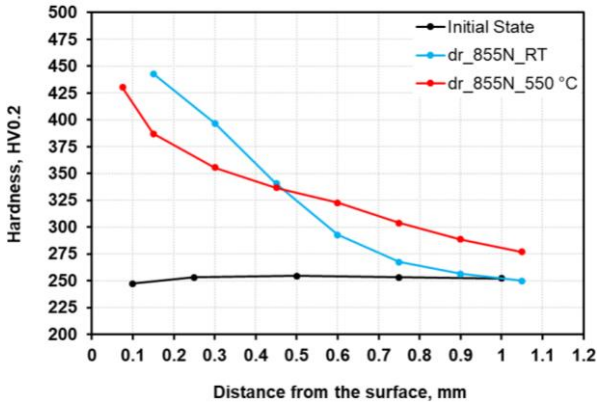

Figure 2. Hardness distribution in the near-surface area after deep rolling at 550 °C using a deep rolling force of 855 N. Data of the initial state condition and of the condition deep rolled at RT using a deep rolling force of 855 N were recompiled from [39].

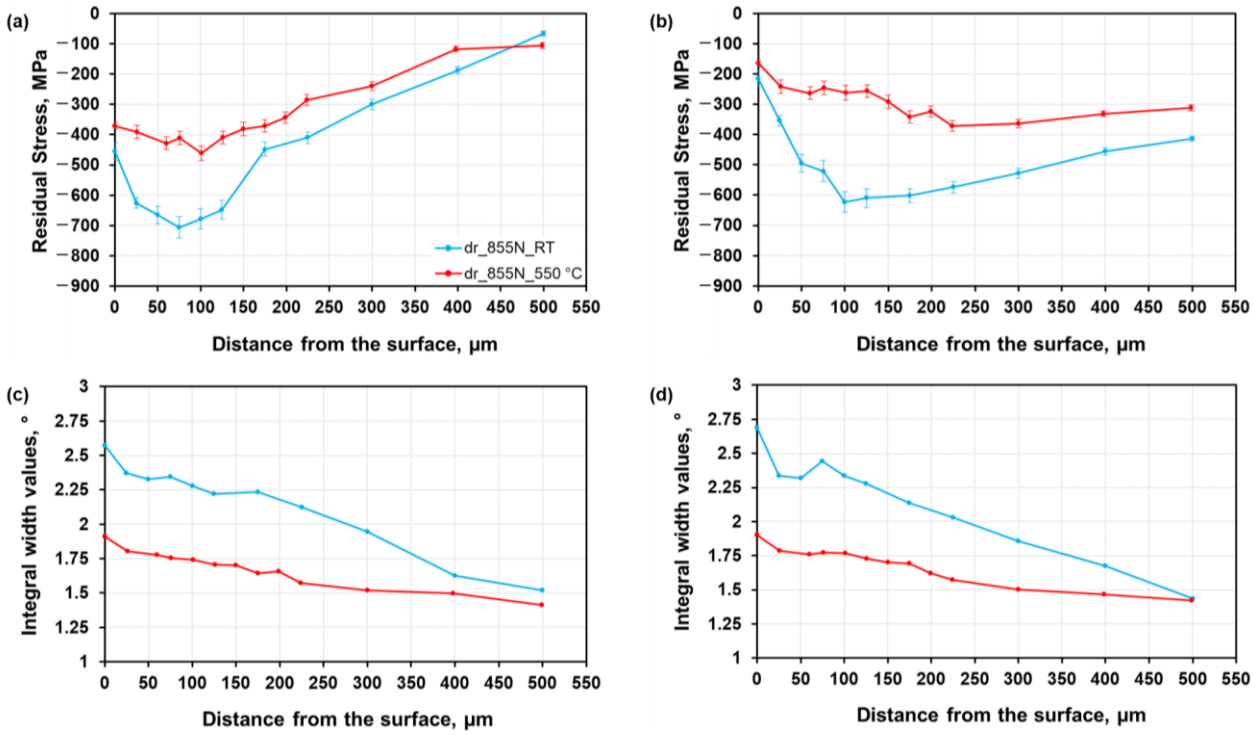

Figure 3. Residual stress profiles and integral width values in longitudinal ((**a**) + (**c**)) and circumferential ((**b**) + (**d**)) directions plotted as a function of deep rolling temperatures at constant deep rolling force. Data of the condition deep rolled at RT using a deep rolling force of 855 N were recompiled from [39].

As is to be expected in this context, the corresponding residual stress profiles depicted in Figure 3a,b also show lower absolute values, with peak longitudinal compressive stresses being approximately −475 MPa for deep rolling at 550 °C compared to −700 MPa for

the dr_855_RT condition. Interestingly, residual stress depth profiles of both conditions considered are characterized by a point of intersection at a similar depth as the hardness depth gradients, i.e., between 400 and 500 µm. At this point, it has to be emphasized that according to the literature [64], XRD residual stress depth profiles recorded applying the layer removal method can be considered as valid when the removal depth is less than one tenth of the diameter of a cylindrical specimen. Considering the diameter of the specimen of 6 mm, as well as the successive effect of layer removal, reliable statements about the residual stress state at large depths can be regarded as doubtful. Thus, in the present work, evaluation of residual stresses and corresponding integral width has only been performed up to a depth of 500 µm. In line with the discussions provided so far, a similar trend can be seen for the circumferential direction, revealing peak values of about −375 and −625 MPa for the dr_855_550 °C and the dr_855_RT conditions, respectively. Compared to the investigations by Oevermann et al. [39], both residual stress and hardness profiles are negatively impacted by an increase of the deep rolling temperature from 200 to 550 °C. As already discussed above, it can be assumed that this indicates the turnaround point, from where on recovery processes and lowered YS outweigh the benefits of higher plastic deformations at elevated temperatures, at least when trying to induce the highest possible residual stress values in the direct vicinity of the surface.

3.2. Material Behavior under Quasistatic and Cyclic Loads

In order to determine the influence of deep rolling temperatures on the macroscopic material behavior, both tensile and HCF tests have been conducted and will be discussed hereafter based on a direct comparison to findings of Oevermann et al. [39] (acting as a benchmark). As depicted in Figure 4 and discussed in [39], both YS and UTS are increased compared to the initial state after deep rolling, irrespective of the process temperature. Here, especially the higher YS is to be considered for the application of high-manganese steels [23]. Comparing the deep rolled conditions with each other, temperature does not seem to have a pronounced effect on the monotonic stress–strain response as the curves of dr_855_550 °C and dr_855_RT only deviate marginally, revealing only slight differences in YS and UTS. In [39], it was shown that deep rolling at 200 °C resulted in an increased YS as compared to the RT deep rolled counterparts. In line with data from hardness measurements shown in Figure 2, a slightly lower YS can be seen for dr_855_550 °C, once again indicating the turnaround point with respect to the elevated process temperatures, as discussed above. Additionally, a decrease in ductility compared to the RT deep rolled specimen can be seen for dr_855_550 °C, following the same trend already seen after deep rolling at 200 °C [39].

During fatigue testing, all deep rolled specimens are characterized by an improved fatigue life in direct comparison to the initial state recompiled from [39], as can be derived from the S-N curves with corresponding trendlines depicted in Figure 5. This observation can be credited to increased YS as well as the compressive residual stresses impeding crack initiation. At lower stress amplitudes, the effect of the strengthened surface layer diminishes consistently. The overall improvement in specimen lifetime is in line with data available in literature for surface-treated austenitic steels and other alloys [65–67]. Notably, the specimens processed at elevated temperatures of 550 °C show a significant increase in fatigue life in comparison to their RT deep rolled counterparts. From the trendlines plotted for dr_855_550 °C and dr_855_RT respectively, being characterized by almost identical slopes, enhancements in fatigue life after deep rolling at an elevated temperature of 550 °C seem to be persistent for all stress amplitudes considered. The results presented by Oevermann et al. [39] revealed that, despite highest compressive residual stresses and depth effect as well as increased YS, UTS and near-surface hardness, increased temperatures of 200 °C during deep rolling only resulted in slightly improved fatigue performances at high stress amplitudes, whereas at lower stress amplitudes, no differences could be identified compared to the RT deep rolled counterparts. In contrast, a further increase of the deep rolling temperature to 550 °C benefits fatigue in the HCF regime by

a constant factor of about 2, as evidenced by the results presented in Figure 5. With the above discussions in mind, this behavior can neither be attributed to higher static strength nor increased residual stresses or surface hardness. In order to rationalize these (at first glance contradicting) results, both fracture surface analysis and residual stress stability tests have been conducted and are discussed in the following.

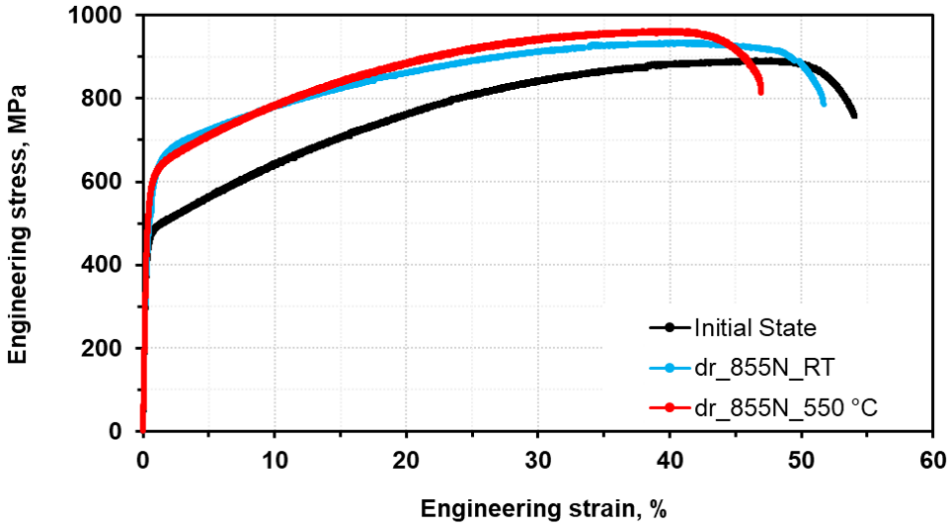

Figure 4. Monotonic stress–strain response of the specimen deep rolled at 550 °C applying a deep rolling force of 855 N. Data of the initial state condition and of the condition deep rolled at RT using a deep rolling force of 855 N were recompiled from [39].

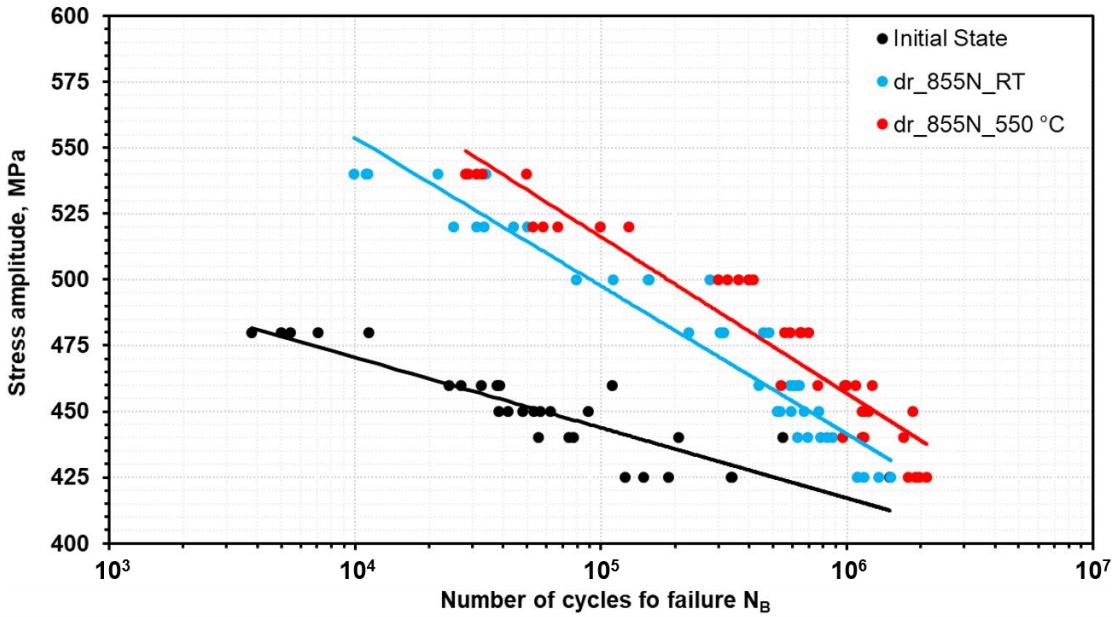

Figure 5. S-N curve of the specimen deep rolled at 550 °C applying a deep rolling force of 855 N. Data of the initial state condition and of the condition deep rolled at RT using a deep rolling force of 855 N were (partly) recompiled from [39].

Figure 6 shows representative post-fatigue fracture surfaces of selected specimens for the dr_855_550 °C condition. Generally, well-known features of a fatigue tested specimen, i.e., areas of crack initiation (marked by the white arrows in the overview images) and propagation as well as a final overload fracture region, can be derived from the micrographs irrespective of the stress level considered. In contrast, differences become obvious with respect to the location of the crack initiation sites depending on the stress level during cyclic

loading. At lower stress amplitudes of 450 and 460 MPa respectively, typical characteristics related to deep rolling known from the literature, i.e., a shift of the crack initiation points away from surface areas towards internal defects as a result of the near-surface compressive residual stresses, become obvious. Thus, crack initiation can clearly be traced back to the marked sites in the interior of the specimens, as further highlighted by the magnified details below the overview images. As no inclusions or pores responsible for fracture initiation can be located at the crack initiation sites, it is assumed that localized embrittlement is a major contributing factor eventually leading to crack initiation in the present study. According to a review by Koyama et al. [68], hydrogen in high-manganese steels is segregated on the phase, grain and twin boundaries, eventually affecting the local properties. In the present study, however, hydrogen-induced crack initiation cannot be clearly proven, and more research is necessary in order to fully understand this topic. At higher stress amplitudes, demonstrated by the fracture surfaces of specimens fatigued at 520 and 540 MPa, respectively, crack initiation is shifted to the surface again, pointing to sufficient plastic strain for the formation of persistent slip bands in the strengthened surface layer. Therefore, it can be assumed that effects shifting the location of crack initiation to the interior of the specimen, such as compressive residual stresses in the surface layer, lose their effect at those increased stress amplitudes. In order to further elucidate these observations, analysis of the residual stress stability was conducted for both the dr_855_RT and the dr_855_550 °C condition.

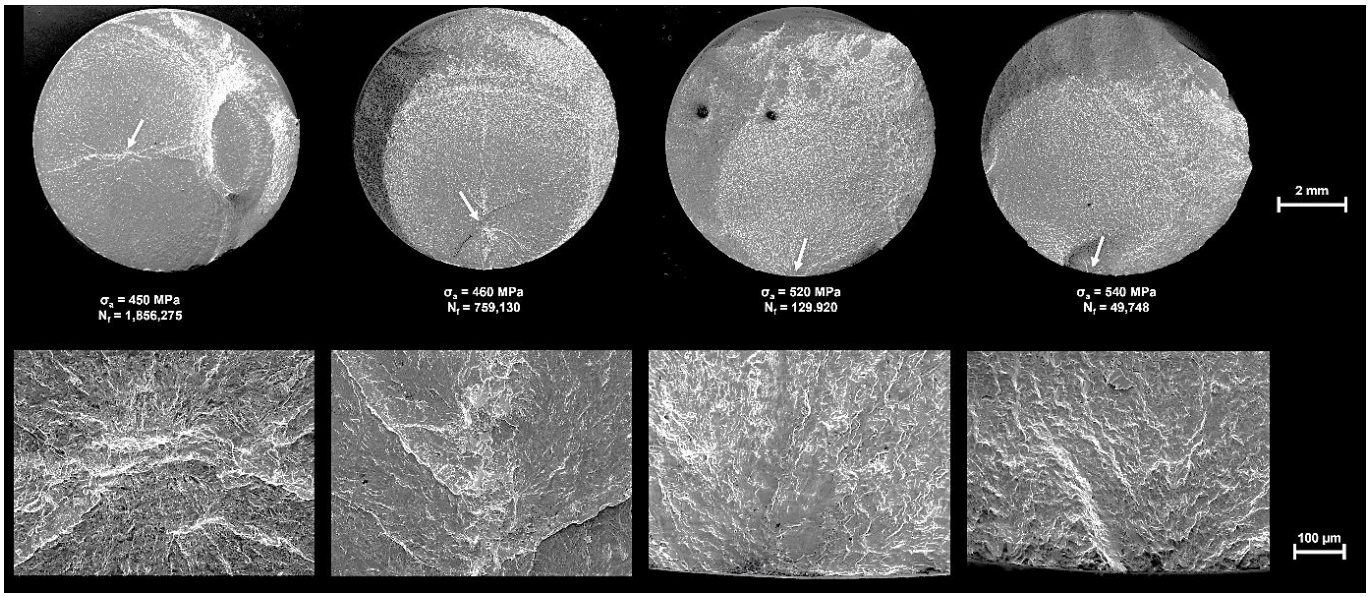

Figure 6. Fracture surfaces of the dr_855N_550 °C condition after cyclic loading at loading amplitudes of 450, 460, 520 and 540 MPa. The pictures below the overview images of the fracture surfaces show magnified details of crack initiation sites marked with white arrows in the overview. For fracture surfaces characterized by multiple crack initiation, only the major site is highlighted and shown in the magnified view.

Figure 7 details pre-fatigue and half-life surface residual stresses in dependence of the applied stress amplitude for specimens deep rolled at RT and 550 °C, respectively. Generally, irrespective of the deep rolling temperature, a decreasing stability of the surface residual stresses can be seen with increasing stress amplitudes (with one exception in Figure 7b). Taking a closer look at the surface residual stress stability of the dr_855_550 °C condition, a significant decrease of 62.1% of the half-life surface residual stress value was only found for the specimen fatigued at the highest stress amplitude of 540 MPa. Specimens tested at lower stress amplitudes showed less degradation in a range between 8.6% and 26.4%, while the lowest relative loss was found for the specimen tested at 460 MPa. Depth profiles in Figure 7d indicate that the trend of very stable residual stresses at low stress amplitudes seems to apply to the whole surface layer, as the specimen tested at 425 MPa

only shows minor deviation compared to the pre-fatigue measurement. Only specimens fatigued at >500 MPa experienced substantial residual stress reduction through plastic deformation, eventually rationalizing the observations revealed by fracture surface analysis. Thus, a degradation in the residual stress stability at stress amplitudes > 500 MPa leads to crack initiation in the direct vicinity of the surface, whereas stable residual stresses result in a shift of the point of crack initiation to the specimen interior.

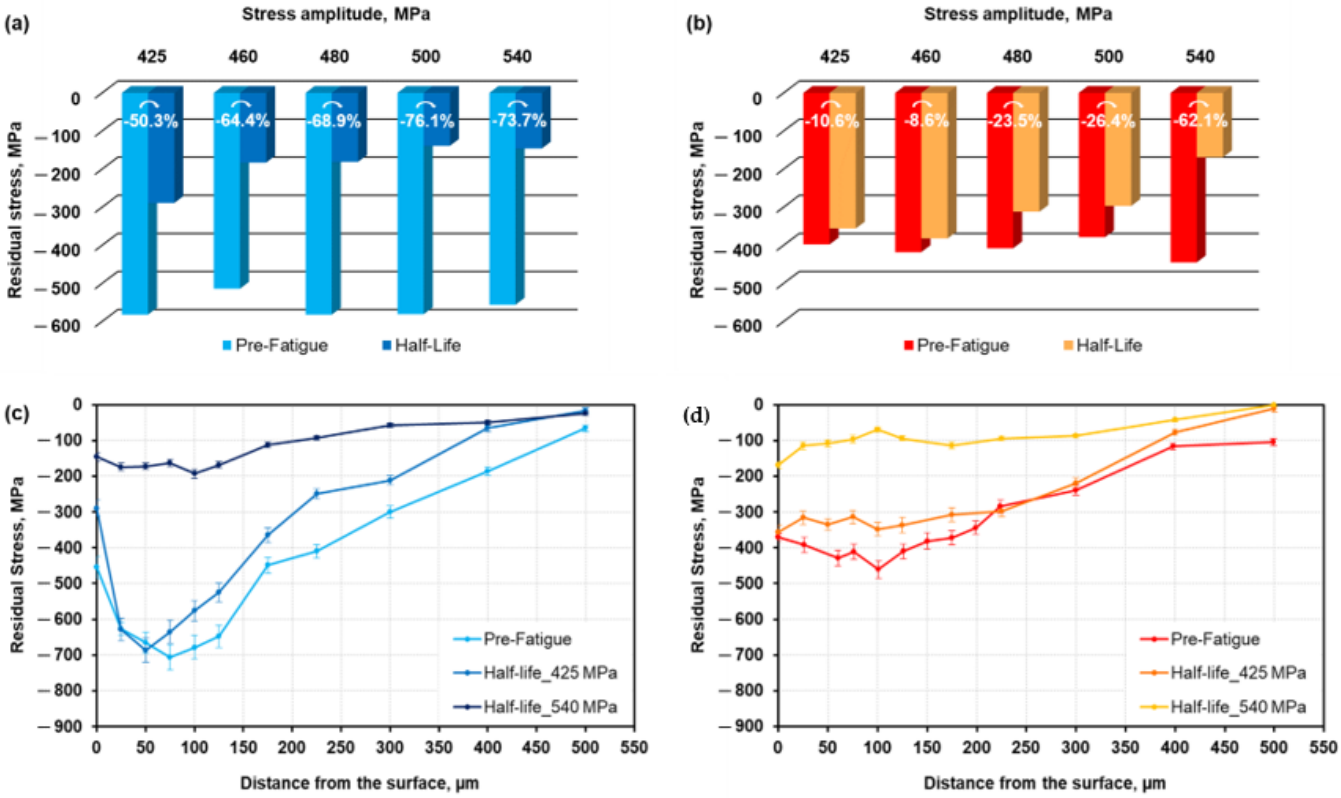

Figure 7. Residual stress stability: Comparison of pre-fatigue and half-life surface residual stress values ($N_B/2$) for varying stress amplitudes and comparison of pre-fatigue and half-life residual stress depth profiles (fatigued at lowest and highest stress amplitude) for ((**a**) + (**c**)) dr_855N_RT and ((**b**) + (**d**)) dr_855N_550 °C condition.

When directly compared to the RT deep rolled specimen, it becomes obvious that microstructure stability is superior for the dr_855_550 °C condition, as the reduction in the surface residual stress for dr_855_RT reaches 50.3% already for the smallest stress level considered, whereas at the highest stress amplitude of 540 MPa, finally, only one quarter of the initial surface residual stress value remains. Nevertheless, it has to be noted that despite a decrease by a factor of approximately 2 in terms of the residual stress value directly at the surface after half-life fatigue (for the lowest stress amplitude of 425 MPa) almost the same maximum value remains, as deduced from the residual stress depth profile depicted in Figure 7c. For the highest stress level, both conditions, i.e., dr_855_RT and dr_855_550 °C, are characterized by similar half-life residual stress depth profiles. In the literature, dynamic strain aging during deep rolling at elevated temperatures is considered to be the major mechanism to increase the microstructural stability of different kinds of steel grades, in turn reducing dislocation movement and annihilation [69,70]. Thus, the aged surface layer microstructure stabilizes the inherent residual stresses to such an extent that fatigue life is measurably increased for the TWIP steel under investigation when compared to non-aged, RT deep rolled specimens. Although the near-surface layer of the dr_855_550 °C condition is characterized by significantly lower hardness and maximum compressive residual stress values, the stability of residual stresses induced by dynamic strain aging effects eventually seems to dominate the fatigue life in the HCF regime (increase up to a factor of 2), as

compared to the RT deep rolled counterparts. However, discussion at that point mainly focused on the direct surface of the specimens, obviously revealing positive effects of dynamic strain aging after deep rolling at 550 °C. In order to further analyze these effects in the bulk of the specimen, evaluation of the plastic strain amplitude, being a measure well-known for having a significant influence on the fatigue behavior, is part of ongoing studies, eventually allowing for additional interpretation of the results shown.

4. Summary and Conclusions

The present work represents a follow-up study to the results shown by Oevermann et al. [39] and was conducted to investigate the consequences of deep rolling at elevated temperature on the near-surface and fatigue properties of the high-manganese TWIP steel X40MnCrAl19-2. Analysis of the surface-treated area was conducted by X-ray diffraction and EBSD, as well as microhardness measurements and uniaxial tensile tests. Additionally, HCF properties studied by means of fully reversed tension-compression tests were critically discussed based on fracture surface appearance and analysis of residual stress stability. From the findings presented, the following conclusions can be drawn:

- EBSD maps of the investigated condition reveal a highly deformed near-surface microstructure, indicating a high dislocation density. Despite the increase in the SFE due to the elevated temperature, deformation-induced twinning can still be seen as a result of the multiaxial stress state induced by deep rolling.
- Deep rolling at 550 °C yields lower hardness and residual stress depth profiles when compared to RT deep rolled counterparts. Obviously, stress relaxation induced by recovery effects appears to outweigh the positive effects of warm deep rolling.
- Despite the nominally lower residual stress values and hardness profiles, specimens deep rolled at elevated temperature are characterized by a noticeable increase in fatigue life due to a stabilized near-surface microstructure. Irrespective of the stress amplitude considered, fatigue properties were improved by a factor of two. As a result, deep rolling at elevated temperatures eventually paves the way for safe and reliable industrial applications of HMnS components being subjected to fatigue loading, such as whishbones in the automotive sector.
- Fractography revealed crack initiation in the interior of the specimen for low- and medium-stress amplitudes, whereas at high-stress amplitudes, cracks were initiated at the direct vicinity of the surface. It is thought that the compressive residual stresses in the surface layer, shifting the location of crack initiation to the interior of the specimen, lose their effect at the increased stress amplitudes.
- Residual stress profiles after half-life fatigue (NB/2) show superior stability after deep rolling at 550 °C compared to RT deep rolled specimens, rationalizing the results obtained based on fatigue and fractography investigations. The superior residual stress stability can be attributed to dynamic strain aging effects.
- Future work should focus on in-depth evaluation of the plastic strain amplitude of the conditions deep rolled at different temperatures in order to further analyze the different elementary effects being active. Additionally, the stability of residual stresses under thermal load should be part of future investigations.

Author Contributions: Conceptualization, T.W.; Methodology, T.W.; Investigation, T.W., M.K. and T.O.; Visualization, T.W.; Writing—Original Draft Preparation, T.W. and M.K.; Writing—Review and Editing, T.W., M.K., T.O. and T.N.; Supervision, T.N.; Project Administration, T.N.; Funding Acquisition, T.W. and T.N. All authors have read and agreed to the published version of the manuscript.

Funding: The present study was funded by "Deutsche Forschungsgemeinschaft" (DFG) (German Research Foundation), Grant No. 406320672, within the research project "Mechanische Oberflächenbehandlung von hochmanganhaltigen TWIP/TRIP Stählen—Mikrostrukturelle Stabilität und mechanische Eigenschaften".

Data Availability Statement: The data presented in this study are available upon request from the corresponding author.

Acknowledgments: The authors would like to thank Rolf Diederich and Rainer Hunke for technical support regarding the maintenance and operation of the laboratory equipment. The assistance of Büsra Demircan is greatly appreciated. The authors acknowledge thyssenkrupp Hohenlimburg GmbH (Hagen, Germany) for providing the material.

Conflicts of Interest: The authors declare no conflict of interest. The funding agency had no influence on the design of the study, the collection, analysis, or interpretation of data, the writing of the manuscript, or the decision to publish the results.

References

1. Fonstein, N. *Advanced High Strength Sheet Steels*; Springer: New York, NY, USA, 2015; pp. 193–195.
2. Kuziak, R.; Kawalla, R.; Waengler, S. Advanced high strength steels for automotive industry. *Arch. Civ. Mech. Eng.* **2008**, *8*, 103–117. [CrossRef]
3. Matlock, D.K.; Speer, J.G. Third Generation of AHSS: Microstructure Design Concepts. In *Arunansu Haldar, Satyam Suwas und Debashish Bhattacharjee (Hg.): Microstructure and Texture in Steels*; Springer: London, UK, 2009; pp. 185–205.
4. Heintzel, A. Leichtbau als Innovationstreiber. *ATZproduktion* **2019**, *6*, 3. [CrossRef]
5. Weidner, A. *Deformation Processes in TRIP/TWIP Steels*; Springer International Publishing: Cham, Switzerland, 2020.
6. De Cooman, B.C.; Kwon, O.; Chin, K.-G. State-of-the-knowledge on TWIP steel. *Mater. Sci. Technol.* **2012**, *28*, 513–527. [CrossRef]
7. Bleck, W.; Phiu-On, K. Microalloying of Cold-Formable Multi Phase Steel Grades. *Mater. Sci. Forum* **2005**, *500–501*, 97–114. [CrossRef]
8. Kwon, O.; Lee, K.Y.; Kim, G.S.; Chin, K.G. New Trends in Advanced High Strength Steel Developments for Automotive Application. *Mater. Sci. Forum* **2010**, *638-642*, 136–141. [CrossRef]
9. Chen, L.; Zhao, Y.; Qin, X. Some aspects of high manganese twinning-induced plasticity (TWIP) steel, a review. *Acta Metall. Sin. (Engl. Lett.)* **2013**, *26*, 1–15. [CrossRef]
10. Grässel, O.; Krüger, L.; Frommeyer, G.; Meyer, L. High strength Fe–Mn–(Al, Si) TRIP/TWIP steels develop-ment—Properties—Application. *Int. J. Plast.* **2000**, *16*, 1391–1409. [CrossRef]
11. Hadfield, R.A. Hadfield's Manganese Steel. *Science* **1888**, *ns-12*, 284–286. [CrossRef]
12. De Cooman, B.C.; Kwang-geun, C.; Jinkyung, K. High Mn TWIP Steels for Automotive Applications. In *Marcello Chiaberge (Hg.): New Trends and Developments in Automotive System Engineering*; InTech: London, UK, 2011.
13. Allain, S.; Chateau, J.-P.; Bouaziz, O.; Migot, S.; Guelton, N. Correlations between the calculated stacking fault energy and the plasticity mechanisms in Fe–Mn–C alloys. *Mater. Sci. Eng. A* **2004**, *387–389*, 158–162. [CrossRef]
14. Bouaziz, O.; Allain, S.; Scott, C.; Cugy, P.; Barbier, D. High manganese austenitic twinning induced plasticity steels: A review of the microstructure properties relationships. *Curr. Opin. Solid State Mater. Sci.* **2011**, *15*, 141–168. [CrossRef]
15. Kim, J.; De Cooman, B.C. On the Stacking Fault Energy of Fe-18 Pct Mn-0.6 Pct C-1.5 Pct Al Twinning-Induced Plasticity Steel. *Metall. Mater. Trans. A* **2011**, *42*, 932–936. [CrossRef]
16. Jin, J.-E.; Lee, Y.-K. Strain hardening behavior of a Fe–18Mn–0.6C–1.5Al TWIP steel. *Mater. Sci. Eng. A* **2009**, *527*, 157–161. [CrossRef]
17. Lee, T.-H.; Shin, E.; Oh, C.-S.; Ha, H.-Y.; Kim, S.-J. Correlation between stacking fault energy and deformation microstructure in high-interstitial-alloyed austenitic steels. *Acta Mater.* **2010**, *58*, 3173–3186. [CrossRef]
18. Dumay, A.; Chateau, J.-P.; Allain, S.; Migot, S.; Bouaziz, O. Influence of addition elements on the stacking-fault energy and mechanical properties of an austenitic Fe–Mn–C steel. *Mater. Sci. Eng. A* **2008**, *483-484*, 184–187. [CrossRef]
19. Hamada, A. *Manufacturing, Mechanical Properties and Corrosion Behaviour of High-Mn TWIP Steels*; Oulu University Press: Oulu, Finland, 2007.
20. Frommeyer, G.; Brüx, U.; Neumann, P. Supra-Ductile and High-Strength Manganese-TRIP/TWIP Steels for High Energy Absorption Purposes. *ISIJ Int.* **2003**, *43*, 438–446. [CrossRef]
21. Remy, L.; Pineau, A. Twinning and strain-induced F.C.C. → H.C.P. transformation in the Fe-Mn-Cr-C system. *Mater. Sci. Eng.* **1977**, *28*, 99–107. [CrossRef]
22. Saeed-Akbari, A.; Mosecker, L.; Schwedt, A.; Bleck, W. Characterization and Prediction of Flow Behavior in High-Manganese Twinning Induced Plasticity Steels: Part I. Mechanism Maps and Work-Hardening Behavior. *Metall. Mater. Trans. A* **2011**, *43*, 1688–1704. [CrossRef]
23. Song, W.; Ingendahl, T.; Bleck, W. Control of Strain Hardening Behavior in High-Mn Austenitic Steels. *Acta Metall. Sin. Lett.* **2014**, *27*, 546–556. [CrossRef]
24. De Cooman, B.C.; Estrin, Y.; Kim, S.K. Twinning-induced plasticity (TWIP) steels. *Acta Mater.* **2018**, *142*, 283–362. [CrossRef]
25. Grajcar, A. Corrosion resistance of high-Mn austenitic steels for the automotive industry. *Corros. Resist.* **2012**, *30*, 353–376. [CrossRef]
26. Chen, S.; Rana, R.; Haldar, A.; Ray, R.K. Current state of Fe-Mn-Al-C low density steels. *Prog. Mater. Sci.* **2017**, *89*, 345–391. [CrossRef]
27. Frommeyer, G.; Brüx, U. Microstructures and Mechanical Properties of High-Strength Fe-Mn-Al-C Light-Weight TRIPLEX Steels. *Steel Res. Int.* **2006**, *77*, 627–633. [CrossRef]
28. Yoo, J.D.; Park, K.-T. Microband-induced plasticity in a high Mn–Al–C light steel. *Mater. Sci. Eng. A* **2008**, *496*, 417–424. [CrossRef]

29. Haase, C.; Zehnder, C.; Ingendahl, T.; Bikar, A.; Tang, F.; Hallstedt, B.; Hu, W.; Bleck, W.; Molodov, D.A. On the deformation behavior of κ-carbide-free and κ-carbide-containing high-Mn light-weight steel. *Acta Mater.* **2017**, *122*, 332–343. [CrossRef]
30. Welsch, E.; Ponge, D.; Haghighat, S.H.; Sandlöbes, S.; Choi, P.; Herbig, M.; Zaefferer, S.; Raabe, D. Strain hardening by dynamic slip band refinement in a high-Mn lightweight steel. *Acta Mater.* **2016**, *116*, 188–199. [CrossRef]
31. Wegener, T.; Haase, C.; Liehr, A.; Niendorf, T. On the influence of $\varkappa$-carbides on the low-cycle fatigue behavior of high-Mn light-weight steels. *Int. J. Fatigue* **2021**, *150*, 106327. [CrossRef]
32. Lee, Y.-K.; Lee, S.-J.; Han, J. Critical assessment 19: Stacking fault energies of austenitic steels. *Mater. Sci. Technol.* **2016**, *32*, 1–8. [CrossRef]
33. Saeed-Akbari, A.; Imlau, J.; Prahl, U.; Bleck, W. Derivation and Variation in Composition-Dependent Stacking Fault Energy Maps Based on Subregular Solution Model in High-Manganese Steels. *Metall. Mater. Trans. A* **2009**, *40*, 3076–3090. [CrossRef]
34. Volosevich, P.U.; Gridnev, V.N.; Petrov, Y.U.N. Influence of Mn and the stacking fault energy of Fe-Mn alloys. In *Physics of Metals and Metallography*; Springer: New York, NY, USA, 1976; Volume 42.
35. Schumann, H. Einfluß der Stapelfehlerenergie auf den kristallographischen Umgitterungsmechanismus der γ/α-Umwandlung in hochlegierten Stählen. *Cryst. Res. Technol.* **1974**, *9*, 1141–1152. [CrossRef]
36. Olson, G.B.; Cohen, M. Kinetics of strain-induced martensitic nucleation. *Metall. Mater. Trans. A* **1975**, *6*, 791–795. [CrossRef]
37. Grässel, O.; Frommeyer, G.; Derder, C.; Hofmann, H. Phase Transformations and Mechanical Properties of Fe-Mn-Si-Al TRIP-Steels. *J. Phys. Colloq.* **1997**, *7*, C5-383–C5-388. [CrossRef]
38. Rüsing, C.J.; Lambers, H.-G.; Lackmann, J.; Frehn, A.; Nagel, M.; Schaper, M.; Maier, H.; Niendorf, T. Property Optimization for TWIP Steels—Effect of Pre-deformation Temperature on Fatigue Properties. *Mater. Today Proc.* **2015**, *2*, S681–S685. [CrossRef]
39. Oevermann, T.; Wegener, T.; Niendorf, T. On the Evolution of Residual Stresses, Microstructure and Cyclic Performance of High-Manganese Austenitic TWIP-Steel after Deep Rolling. *Metals* **2019**, *9*, 825. [CrossRef]
40. Mughrabi, H. Cyclic Slip Irreversibilities and the Evolution of Fatigue Damage. *Metall. Mater. Trans. A* **2009**, *40*, 431–453. [CrossRef]
41. Skorupski, R.; Smaga, M.; Eifler, D. Influence of Surface Morphology on the Fatigue Behavior of Metastable Austenitic Steel. *Adv. Mater. Res.* **2014**, *891–892*, 464–469. [CrossRef]
42. Kumar, D.; Idapalapati, S.; Wang, W.; Narasimalu, S. Effect of Surface Mechanical Treatments on the Microstruc-ture-Property-Performance of Engineering Alloys. *Materials* **2019**, *12*, 2503. [CrossRef] [PubMed]
43. Delgado, P.; Cuesta, I.; Alegre, J.M.; Díaz, A. State of the art of Deep Rolling. *Precis. Eng.* **2016**, *46*, 1–10. [CrossRef]
44. Schulze, V. *Modern Mechanical Surface Treatment—States, Stability, Effects*; WILEY-VCH Verlag GmbH & Co. KGaA: Weinheim, Germany, 2006.
45. Teichmann, C.; Wagner, L. Shot peening of TWIP steel—Influence on mechanical properties. In Proceedings of the ICSP-12, Goslar, Germany, 15–18 September 2014; pp. 499–503.
46. Kongthep, J.; Timmermann, K.; Scholtes, B.; Niendorf, T. On the impact of deep rolling at different temperatures on the near surface microstructure and residual stress state of steel AISI 304. *Mater. und Werkst.* **2019**, *50*, 788–795. [CrossRef]
47. Oevermann, T.; Wegener, T.; Liehr, A.; Hübner, L.; Niendorf, T. Evolution of residual stress, microstructure and cyclic performance of the equiatomic high-entropy alloy CoCrFeMnNi after deep rolling. *Int. J. Fatigue* **2021**, *153*, 106513. [CrossRef]
48. James, N. Residual stress influences on structural reliability. *Eng. Fail. Anal.* **2011**, *18*, 1909–1920. [CrossRef]
49. Hensel, J.; Nitschke-Pagel, T.; Dilger, K. Effects of residual stresses and compressive mean stresses on the fatigue strength of longitudinal fillet-welded gussets. *Weld. World* **2016**, *60*, 267–281. [CrossRef]
50. Gadallah, R.; Osawa, N.; Tanaka, S.; Tsutsumi, S. Critical investigation on the influence of welding heat input and welding residual stress on stress intensity factor and fatigue crack propagation. *Eng. Fail. Anal.* **2018**, *89*, 200–221. [CrossRef]
51. Syed, A.K.; Ahmad, B.; Guo, H.; Machry, T.; Eatock, D.; Meyer, J.; Fitzpatrick, M.E.; Zhang, X. An experimental study of residual stress and direction-dependence of fatigue crack growth behaviour in as-built and stress-relieved selec-tive-laser-melted Ti6Al4V. *Mater. Sci. Eng. A* **2019**, *755*, 246–257. [CrossRef]
52. Wu, S.; Luo, Y.; Shen, Z.; Zhou, L.; Zhang, W.; Kang, G. Collaborative crack initiation mechanism of 25CrMo4 alloy steels subjected to foreign object damages. *Eng. Fract. Mech.* **2020**, *225*, 106844. [CrossRef]
53. Perić, M.; Nižetić, S.; Garašić, I.; Gubeljak, N.; Vuherer, T.; Tonković, Z. Numerical calculation and experimental measure-ment of temperatures and welding residual stresses in a thick-walled T-joint structure. *J. Therm. Anal. Calorim.* **2020**, *141*, 313–322. [CrossRef]
54. Nitschke-Pagel, T. Recommendations for the measurement of residual stresses in welded joints by means of X-ray diffraction—Results of the WG6-RR test. *Weld. World* **2020**, *65*, 1–12. [CrossRef]
55. Klein, M.W.; Blinn, B.; Smaga, M.; Beck, T. High cycle fatigue behavior of high-Mn TWIP steel with different surface mor-phologies. *Int. J. Fatigue* **2020**, *134*, 105499. [CrossRef]
56. Klein, M.W.; Smaga, M.; Beck, T. Surface Morphology and Its Influence on Cyclic Deformation Behavior of High-Mn TWIP Steel. *Metals* **2018**, *8*, 832. [CrossRef]
57. Torabi, S.A.; Amini, K.; Gharavi, F. The effect of shot peening and precipitation hardening on the wear behavior of high manganese austenitic steels. *Metall. Res. Technol.* **2017**, *114*, 507. [CrossRef]
58. Nikitin, I.; Besel, M. Residual stress relaxation of deep-rolled austenitic steel. *Scr. Mater.* **2008**, *58*, 239–242. [CrossRef]

59. Lee, H.; Mall, S. Stress relaxation behavior of shot-peened Ti–6Al–4V under fretting fatigue at elevated temperature. *Mater. Sci. Eng. A* **2004**, *366*, 412–420. [CrossRef]
60. John, R.; Buchanan, D.J.; Caton, M.J.; Jha, S.K. Stability of shot peen residual stresses in IN100 subjected to creep and fatigue loading. *Procedia Eng.* **2010**, *2*, 1887–1893. [CrossRef]
61. Holzapfel, H.; Schulze, V.; Vöhringer, O.; Macherauch, E. Residual stress relaxation in an AISI 4140 steel due to quasistatic and cyclic loading at higher temperatures. *Mater. Sci. Eng. A* **1998**, *248*, 9–18. [CrossRef]
62. Eigenmann, B.; Schulze, V.; Vohringer, O. Surface Residual Stress Relaxation in Steels by Thermal or Mechanical Treatment. In Proceedings of the 4th International Conference on Residual Stresses, Baltimore, MD, USA, 8–10 June 1994; pp. 598–607.
63. Rüsing, C.J. Optimierung der Monotonen und Zyklischen Eigenschaften von Hoch Manganhaltigen TWIP-Stählen: Einfluss von Temperatur und Vorverformung auf die Mikrostrukturentwicklung: Universitätsbibliothek. 2015. Available online: https://books.google.de/books?id=-HMMyAEACAAJ (accessed on 16 October 2021).
64. Moore, M.G.; Evans, W.P. Mathematical Correction for Stress in Removed Layers in X-ray Diffraction Residual Stress Analysis. In *SAE Technical Paper Series*; Pre-1964 SAE Technical Papers; SAE International: Warrendale, PA, USA, 1906.
65. Nikitin, I.; Scholtes, B. Deep rolling of austenitic steel AISI 304 at different temperatures—Near surface microstructures and fatigue. *HTM J. Heat Treat. Mater.* **2012**, *67*, 188–194. [CrossRef]
66. Saalfeld, S.; Krochmal, M.; Wegener, T.; Scholtes, B.; Niendorf, T. On the fatigue behavior of differently deep rolled condi-tions of SAE 1045 in the very-high-cycle fatigue regime. *Int. J. Fatigue* **2021**, *151*, 106360. [CrossRef]
67. McCLUNG, R.C. A literature survey on the stability and significance of residual stresses during fatigue. *Fatigue Fract. Eng. Mater. Struct.* **2007**, *30*, 173–205. [CrossRef]
68. Koyama, M.; Akiyama, E.; Lee, Y.-K.; Raabe, D.; Tsuzaki, K. Overview of hydrogen embrittlement in high-Mn steels. *Int. J. Hydrogen Energy* **2017**, *42*, 12706–12723. [CrossRef]
69. Angkurarach, L.; Juijerm, P. Effects of High-Temperature Deep Rolling on Fatigue, Work Hardening, and Residual Stress Relaxation of Martensitic Stainless Steel AISI *J. Mater. Eng. Perform.* **2020**, *29*, 1416–1423. [CrossRef]
70. Altenberger, I.; Nikitin, I.; Scholtes, B. Static and dynamic strain aging of deep-rolled plain carbon steel SAE 1045 for opti-mized fatigue strength. In Proceedings of the 9th International Conference on Shot Peening, Paris, France, 6–9 September 2005; Schulze, V., Niku-Lari, A., Eds.; IITT-International: Paris, France, 2005; pp. 253–260.